Journal of Materials Chemistry A



PAPER

View Article Online
View Journal | View Issue



Cite this: *J. Mater. Chem. A*, 2023, **11**, 12992

Highly controllable and reproducible one-step synthesis of β -NaYF₄:Er³⁺@NaYbF₄@NaYF₄ upconversion nanoparticles for Sb₂(S,Se)₃ solar cells with enhanced efficiency†

Xin Jin,^a Shin Woei Leow,^a Yanan Fang^a and Lydia Helena Wong (1) **ab

Using multilayer structures of upconversion nanophosphors is widely considered an effective and necessary strategy to achieve efficient luminescence. However, the synthesis of high-quality upconversion nanoparticles in a controllable and reproducible manner remains a challenge, especially for the monodisperse growth of core–shell–shell nanocrystals. Herein, we present a well-designed heating strategy that realizes the one-step synthesis of a hexagonal NaYF₄ host with ideal particle size and shape and further enables us to accomplish the successive growth of a spherical core containing an activator and conformal dual shells containing a sensitizer. In particular, we discuss the upconversion luminescence mechanism of Yb³⁺/Er³⁺ co-doped nanoparticles in detail, which were further introduced into Sb₂(S,Se)₃ solar cells as an extra light harvester, yielding a nominal power conversion efficiency of 9.17%. The present work helps to further clarify the effect of thermal conditions on the crystal growth and luminescence properties of upconversion nanoparticles, which is important for their practical applications.

Received 13th January 2023 Accepted 4th April 2023

DOI: 10.1039/d3ta00241a

rsc.li/materials-a

10th anniversary

Congratulations to the *J. Mater. Chem. A* on its important 10th anniversary milestone. We have been loyal JMCA submitters from its inception and have been avidly following its published articles that cover a diverse range of scientific research on materials for energy and sustainability. It is thrilling to be part of the growth and success of *J. Mater. Chem. A* over the past decade. We extend our best wishes to *J. Mater. Chem. A* for continued success in the decades to come and eagerly anticipate collaborating on and reading more exceptional publications from this esteemed journal.

Introduction

Photon upconversion (UC) materials with the ability to convert low-energy near-infrared (NIR) excitation to high-energy visible emission have been a hot topic in materials science given their potential applications, mainly in laser physics and bioimaging,1-4 and more recently, in photovoltaics.⁵⁻⁹ Among UC materials, lanthanide (Ln)-doped upconversion nanoparticles (UCNPs) were widely studied for their high chemical stability, long excited state lifetime and sharp emission bandwidth.10 With the rapid development of nanoscience, a variety of Ln-doped UCNPs have been successfully synthesized based on different routes, such as solvothermal, hydrothermal and thermal decomposition methods. 11-14 In particular, hexagonal NaYF₄ (β phase) possesses lower phonon energy than cubic $NaYF_4$ (α phase) and is considered one of the most efficient host materials for green/red upconversion from the combination of trivalent Yb^{3+} sensitizer and Er^{3+} activator under NIR excitation. ^{15,16}

However, in order to avoid concentration quenching effects, low doping concentrations of activator ions and sensitizer ions are usually adopted,17 while surface quenching caused by surface defects and solvent adsorption cannot be ignored. 18,19 All of these factors together suppress the quantum yield (QY) of UCNPs and become the biggest problem for their practical application. To date, some schemes have been proposed to solve this problem, such as epitaxial growth of core-shell nanostructures and spatial separation strategies.20-22 Among them, Liu et al. innovatively proposed novel core-shell-shell structured UCNPs of NaYF4@NaYbF4:8%Er@NaYF4, starting from the synthesis of a small-sized α-NaYF₄ core, and pointed out that a high sensitizer content as well as an inert shell are important for upconversion luminescence (UCL).23 Recently, a modified core-shell-shell structure of β-NaYF₄:10% Er@NaYbF4@NaYF4 was successfully employed for UCNPs by

[&]quot;School of Materials Science and Engineering, Nanyang Technological University, Singapore 639798, Singapore. E-mail: lydiawong@ntu.edu.sg

^bCampus for Research Excellence and Technological Enterprise (CREATE), 1 Create Way, 139602, Singapore

Zhou et al. where the core containing Er3+ activator ions was converted from its α phase based on a two-step ripening process and spatially separated from the Yb3+ sensitizer in the shell. This ingenious design effectively breaks the limits of the concentration quenching issue and achieved a high QY of 6.82% at low excitation power density levels.21 The aforementioned progress provides ample evidence that an elaborated structural design along with rational elemental distribution of lanthanides is important for UCNPs to achieve intense luminescence efficiency. What's more, a two-step synthesis strategy of growing β-NaYF₄ crystals from α-NaYF₄ precursors by Ostwald-ripening is widely accepted for better control of particle size and shape, but this usually requires a longer preparation cycle. 19,24,25 Despite the recent advances that have given a strong impetus to the development of upconversion techniques, the synthesis of high-quality UCNPs with specific sizes and morphologies in a facile manner remains a challenge. This is especially the case for multilayered core-shell-shell structures, which is usually caused by the use of complex technical schemes or indiscriminate parameter settings during the preparation process. In addition, the promising design of spatial separation of the activator and sensitizer in the core and shell for mitigating the concentration quenching effect also needs more exploration and validation.

In addition, as an important application direction for UCNPs, there have been many studies exploring the use of UCNPs to collect near-infrared solar photons and then absorb the emitted high-energy photons to generate additional photocurrent for solar cells. It is well known that the AM 1.5G spectrum covers a wide range of photons from ultraviolet to infrared wavelengths, but single-junction solar cells are able to utilize only a fraction of the spectrum due to their defined band gap. In principle, photons with energy below the band gap (absorption threshold) are not absorbed, which is a fundamental factor limiting device efficiency. Introducing upconversion nanomaterials with spectral conversion capabilities into solar cells is a very promising strategy for efficiency enhancement beyond the conventional Schockley-Quisser limit. UCNPs are usually placed on the back side of the device substrate or in the electron transport or light harvesting layers, 8,26-28 which require additional processing to make their combination work well. Therefore, there is an urgent need to explore a new combination strategy that will simplify the device preparation process as well as improve process reproducibility.

In this study, we aim to provide a one-step synthesis strategy to prepare core-shell-shell structured UCNPs with controllable particle shape and size. The influence of thermal conditions on crystal growth properties and luminescent properties has been investigated in detail. We also show that UCL emission can be shifted synchronously from green to blue and red by simply replacing the activator ions based on the current synthetic strategy. Furthermore, considering the inherent ability of UCNPs to convert near-infrared light to visible light, we further incorporated Yb3+/Er3+ co-doped UCNPs into n-i-p Sb2(S,Se)3 thin film solar cells which is a very promising next-generation thin-film solar cell technology with an absorption threshold of about 800 nm. We believe that the power conversion efficiency

can be improved by obtaining additional photocurrent originating from the upconversion process.

Results and discussion

Synthesizing lanthanide-doped UCNPs with a core-shell-shell structure

It is well known that NaYF4 naturally crystallizes as a cubic phase (α-NaYF₄) or a hexagonal phase (β-NaYF₄), as shown in Fig. 1a, depending on the crystal growth conditions. Furthermore, many studies have shown that β-NaYF₄ is able to provide a more efficient host lattice for the accommodation of lanthanide ions compared to the cubic one and therefore usually vields a higher upconversion QY. In view of this, it is necessary to first clarify the effect of synthesis conditions on the crystal growth of NaYF4. The detailed synthesis procedures of the nanocrystals can be found in the Experimental section. Fig. 1b depicts the typical temperature profile for growing NaYF4, which contains three heating zones: a low temperature stage $(t_{\rm zonel} < 100 \, {\rm ^{\circ}C})$ used for removing most of the impurities such as water and air, a second medium temperature stage (100 °C < $t_{\rm zoneII}$ < 150 °C) for further eliminating tightly adsorbed residues, and a third high temperature stage ($t_{\text{zoneIII}} > 260 \, ^{\circ}\text{C}$) for crystal growth. As shown in Fig. 1c, the structural information of the corresponding products was determined by X-ray diffraction (XRD). It can be seen that nanoparticles grown at a relatively low temperature of 280 °C in zone III tend to crystallize into the α phase (profile 1), as reflected by the diffraction peaks at 28.44°, 32.89°, 47.01° and 55.72°, corresponding to the (111), (200), (220) and (311) planes of cubic NaYF₄ (JCPDS No. 06-0342), respectively. In contrast, nanoparticles prepared at a higher growth temperature of 320 °C (temperature profiles 2, 3 and 4) have hexagonal structures (JCPDS No. 16-0334).

Furthermore, we found that the thermal history in zones I and II has a significant impact on the final shape of NaYF4 crystals. As shown in Fig. S2b and c,† the lower temperature in zone II leads to uncontrolled crystal growth and irregular shapes (temperature profile 2), while omitting zone I directly leads to the formation of large hexagonal nanoprisms (temperature profile 4). In comparison, NaYF4 crystals prepared with temperature profile 3 produced regularly shaped particles and a narrow size distribution (Fig. S2d†). We believe that the thermal history regulates the complexation state of the metal ions with the solvent and impurity molecules, thus affecting the subsequent nucleation and growth behaviour of the nanocrystals. Hence, temperature profile 3 is determined to be the optimal heating strategy for the synthesis of β-NaYF₄ crystals. Based on temperature profile 3, we further investigated the effect of growth time on the crystal morphology as shown in Fig. S2d-f.† It can be seen that as the reaction time increases, besides an increase in particle size, the final morphology gradually transitions from spherical to hexagonal nanoplates and further forms nanorods. This indicates that the NaYF4 crystals tend to grow anisotropically at higher temperatures, i.e., promoting the longitudinal growth of the crystals along the caxis.

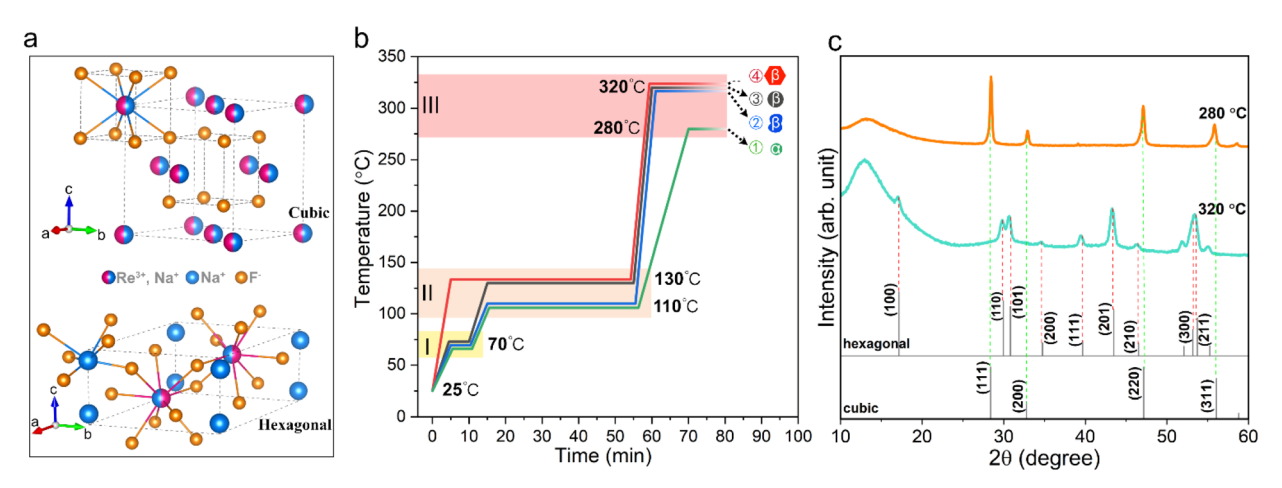


Fig. 1 (a) Schematic diagram of the crystal structure of cubic and hexagonal NaYF₄. (b) Temperature profiles used for synthesizing UCNPs during the thermal decomposition process. (c) XRD patterns of NaYF₄ nanoparticles synthesized at growth temperatures of 280 °C and 320 °C.

In addition, many studies have shown that the formation of $\beta\textsc{-NaYF}_4$ crystals involves a transition process from the metastable intermediate phase of $\alpha\textsc{-NaYF}_4$ to the thermodynamically stable phase of $\beta\textsc{-NaYF}_4.^{29,30}$ In this study, a one-step synthesis strategy was demonstrated to grow $\beta\textsc{-NaYF}_4$ nanoparticles efficiently and conveniently with good control over the shape and size of nanoparticles. The main reason is proposed to be the high heating rate between zones II and III, reaching 45 °C min $^{-1}$, which caused a rapid increase in the growth temperature from 250 °C to 320 °C in just 1.5 min, where the former was identified as the temperature point at which the metal precursor of trifluoroacetic acid starts to decompose

substantially in solution. Although we cannot exclude the possibility that the intermediate α phase is transformed into the stable β phase at elevated temperatures, the high concentration of monomers originating from the rapid decomposition of metal trifluoroacetate acts as a powerful driving force that facilitates the rapid formation of hexagonal phase seeds at the initial reaction stage, thus growing the desired β -NaYF $_4$ crystals in such a short period of time.

Based on the above exploration, we decided to adopt the optimal heating strategy to grow UCNPs with the core-shell-shell structure of NaYF₄:10%Er³⁺@NaYbF₄@NaYF₄, in which the emitter and sensitizer are spatially separated and placed in

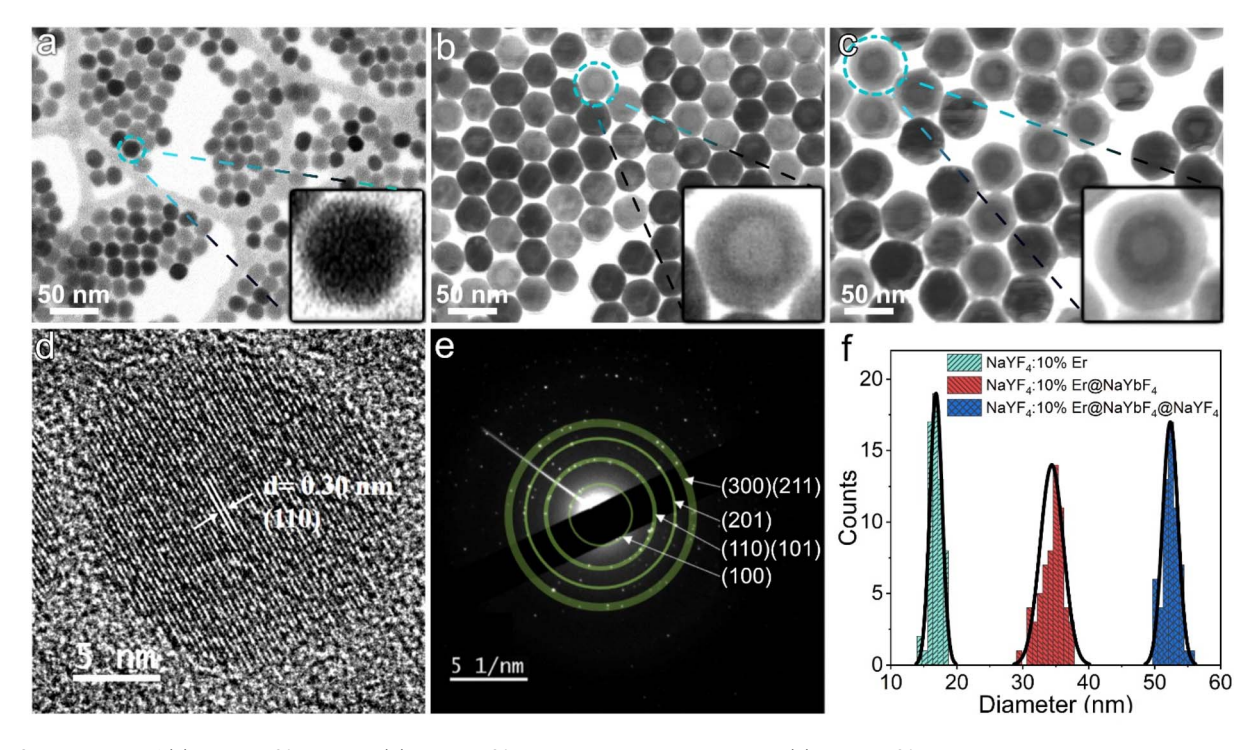


Fig. 2 SEM images of (a) NaYF₄:10%Er core, (b) NaYF₄:10%Er@NaYbF₄ core—shell, and (c) NaYF₄:10%Er@NaYbF₄@NaYF₄ core—shell—shell. (d) HRTEM image of a single NaYF₄:10%Er core and (e) the corresponding SAED pattern. (f) Particle size statistics based on SEM images.

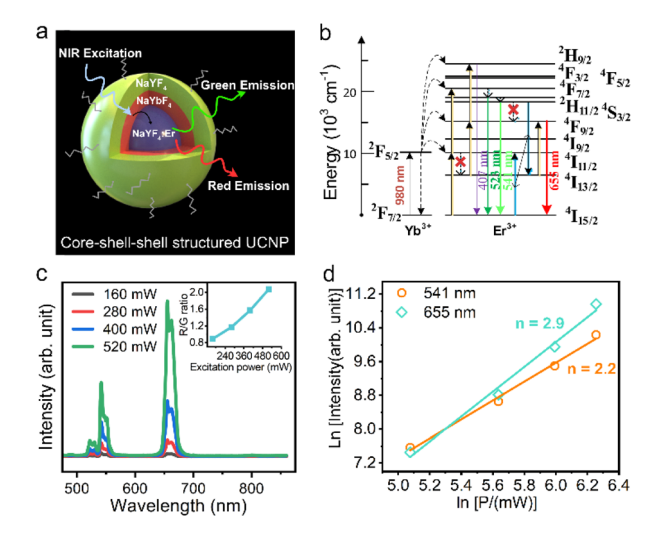


Fig. 3 (a) Schematic diagram showing the emission properties of UCNPs, (b) schematic illustration of the proposed energy transfer mechanism, (c) power-dependent emission spectra and (d) the relationship between emission intensity and excitation power of coreshell-shell structured NaYF4:10%Er@NaYbF4@NaYF4 UCNPs.

the core and shell, respectively. Such a configuration has been shown to not only help increase the upper concentration limit of the Er3+ emitter, but also alleviate the cross-relaxation between the Er3+ emitter and the Yb3+ sensitizer.21 In addition, the outermost NaYF4 shell effectively shields against adverse interference from the solvent environment. This multilayer structure of UCNPs was grown sequentially. First, the NaYF₄:10%Er core was prepared based on temperature profile 3 with a growth time of 20 min. The inner and outer shells were subsequently prepared using a modified temperature profile with the growth temperature and growth time adjusted to 300 ° C and 10 min, respectively.

Fig. 2a shows the morphology of the NaYF4:10%Er core collected by SEM operating in transmission electron diffraction (TED) mode. As shown in the inset, the individual nanoparticles have fuzzy hexagonal outlines. Fig. 2d shows the highresolution TEM (HRTEM) image of a single nanoparticle, demonstrating clear lattice stripes. The measured d-spacing of 0.30 nm corresponds to the (110) plane of the β phase. The selected area electron diffraction (SAED) pattern (Fig. 2e) shows a series of polycrystalline diffraction rings originating from the (100), (110)/(101), (201) and (300)/(211) planes, in agreement with the XRD results, proving the β phase nature of the Lndoped core. Fig. 2b and c present the morphology of the UCNPs with the inner and outer shells epitaxially grown on the core, respectively, and it can be seen that the multilayer nanoparticles still maintain good monodispersity and regularity. Since Y³⁺ and Yb³⁺ have different atomic numbers, they are detected as contrasting light and dark zones in the bright field scanning transmission electron microscopy images. The formation of core-shell and core-shell-shell is clearly visible in Fig. 2b and c and suggests that the present synthetic strategy is capable of achieving conformal epitaxial growth with dual shells. Here, 60 nanoparticles per sample were randomly

selected for size counting. As shown in Fig. 2f, the core diameter, inner shell thickness and outer shell thickness of the prepared UCNPs were calculated to be 17 nm, 9 nm and 9 nm, respectively. This overall size makes them suitable for some specific electronic device applications, such as thin-film solar cells. At this point, we can conclude that the heating strategy adopted in this study can provide highly stable and controlled thermodynamic conditions for the growth of multilayer nanocrystals, thus ensuring the efficient preparation of UCNPs with the desired shape and size. To demonstrate its universality, we tried several other lanthanide ion combinations in UCNPs with core-shell structures, including NaYF₄:10% Tm@NaYbF4 and NaYF4:10%Ho@NaYbF4:40%Ce, which are in excellent dispersion and emit intense blue and red light, respectively, as shown in Fig. S3.†

Study on upconversion luminescence properties

As illustrated in Fig. 3a, Yb³⁺ and Er³⁺ co-doped β-NaYF₄ is widely proven to be an efficient upconversion phosphor, emitting strong green/red light under NIR excitation. Among them, the green emission is considered a two-photon process, which involves resonant energy transfer (ET) and phonon-assisted relaxation. Fig. 3b shows the corresponding energy level diagram of Yb3+ and Er3+, where Yb3+ can be excited from the ²F_{7/2} ground state to the ²F_{5/2} excited state by absorbing a NIR photon and then transferring its energy to Er3+ ions through a resonant ET process, which forces the electron in Er³⁺ to transit from the 4I15/2 ground state into 4I11/2 excited states. Subsequently, Er³⁺ gains energy from the neighbouring Yb³⁺ ion via the ET process again and the higher ⁴F_{7/2} excited state can be further populated, followed by non-radiative relaxation to lower ²H_{11/2} and ⁴S_{3/2} states. Finally, green light can be emitted by radiative transition from the excited ²H_{11/2} and ⁴S_{3/2} states into the ⁴I_{15/2} ground state. The above discussion is demonstrated in our study. As shown in the power-dependent UCL spectra (Fig. 3c), it is clear that three emission peaks centered at 522, 541 and 655 nm appear on each spectrum, corresponding to the green emission of ${}^2H_{11/2}$ – ${}^4I_{15/2}$ and ${}^4S_{3/2}$ – ${}^4I_{15/2}$ and red emission of ${}^4\mathrm{F}_{9/2}{}^{-4}\mathrm{I}_{15/2}$ from Er^{3+} ions, respectively. It should be noted here that the observed broadening of the emission peaks is a consequence of the overlap of the closed sub-energy levels caused by the Stark splitting of the corresponding energy levels, which is common in rare-earth ion-doped upconversion materials.31,32

Fig. 3d plots the double logarithmic curve of the emission intensity versus excitation power for calculating the number of photons involved in the UCL process. For the green emission, the value is determined to be 2.2, which is in agreement with the twophoton excitation theory described above. However, the red emission corresponds to a value of 2.9, which suggests the existence of a three-photon upconversion process in our core-shellshell structured UCNPs and directly rules out the possibility of two previously proposed two-photon theories that the fundamental ⁴F_{9/2} for red emission can be populated by either a multiphonon relaxation process from the initially pumped ⁴S_{3/2} green emitting state or a multiphonon assisted relaxation from the 4I11/

 $_2$ excited state to a lower $^4\mathrm{I}_{13/2}$ state followed by ET-driven transition.

More importantly, we note here that the intensity ratio of red to green light increases monotonically with increasing excitation power, as shown in the inset of Fig. 3c. This phenomenon can also be visualized in the luminescence photograph (Fig. S4†), where the emitted light gradually switches from green to yellow and red as the excitation power density increases. This supports the proposition that red emission is produced from a three-photon process, and the generation route is closely intertwined with the green UCL process. In addition, the high doping concentration (10% Er³⁺) of the core in this study should also be considered. Based on these conditions, we suggest that there exists a cross-relaxation process involved in the red emission. As shown in Fig. 3b, after the initial population of ${}^4S_{34}$ 2 green emitting states by two consecutive ET processes and subsequent nonradiative relaxation, the ${}^4\mathrm{I}_{13/2}$ reservoir state can be populated through a cross-relaxation process between two adjacent Er^{3+} ions ${}^4S_{3/2} + {}^4I_{15/2} \rightarrow {}^4I_{13/2} + {}^4I_{11/2}$, which further populates the ⁴F_{9/2} red emitting state and finally the red light is released via radiative transition to the ⁴I_{15/2} ground state. The above explanation of cross-relaxation is reasonable if we consider the following two pieces of evidence: (1) the population of the intermediate 4I13/2 state used for red emission is at the expense of preestablished ⁴S_{3/2} green emitting states, which is consistent with the experimentally observed increase in the R/Gratio; (2) the high Er³⁺ doping concentration and higher excitation power can provide closer atomic distances and more excited states to promote the cross-relaxation.

Application of UCNPs in solar cells

As shown in Fig. S5a,† we realized that the emission spectrum of the prepared NaYF₄:10%Er³⁺@NaYbF₄@NaYF₄ material matches well with the optical absorption of inorganic antimony sulfoselenide (Sb₂(S,Se)₃), where the latter is a very promising material for next generation solar cells. Therefore, we tried to embed the as-prepared UCNPs into Sb₂(S,Se)₃ cell devices to enhance the photocurrent (Fig. 4a). The electrical properties of the reference cell and its corresponding cross-sectional SEM image are shown in Fig. S6.†

Since the synthesized UCNPs have a small amount of surfactant (oleic acid) adsorbed on their surface, it can be easily comixed with commercial Spiro-OMeTAD in chlorobenzene solution, which enables the preparation of a bifunctional hole transport layer with a smooth and dense surface, as shown in Fig. 4b. The mixed solution emitted red light under 980 nm laser excitation (Fig. S5b†). In addition, theoretical studies suggest that a promising way to promote the contribution of upconversion luminescence to photocurrent is to operate the solar cell under concentrated irradiation.33 Therefore, we tested the solar cell performance with either AM1.5 illumination, a 980 nm NIR laser (\sim 800 mW) or a combination of both. We first performed a NIR response test under the combined irradiation of sunlight and a 980 nm laser, as shown in Fig. 4c. The NIR laser source was turned off and on alternately. The fluctuation in current indicates that the solar cell responds well to the laser signal with the help of UCNPs. Fig. 4d shows the *I-V* characteristics of a solar cell device under laser, sunlight and their combination. Compared with the reference device (Fig.

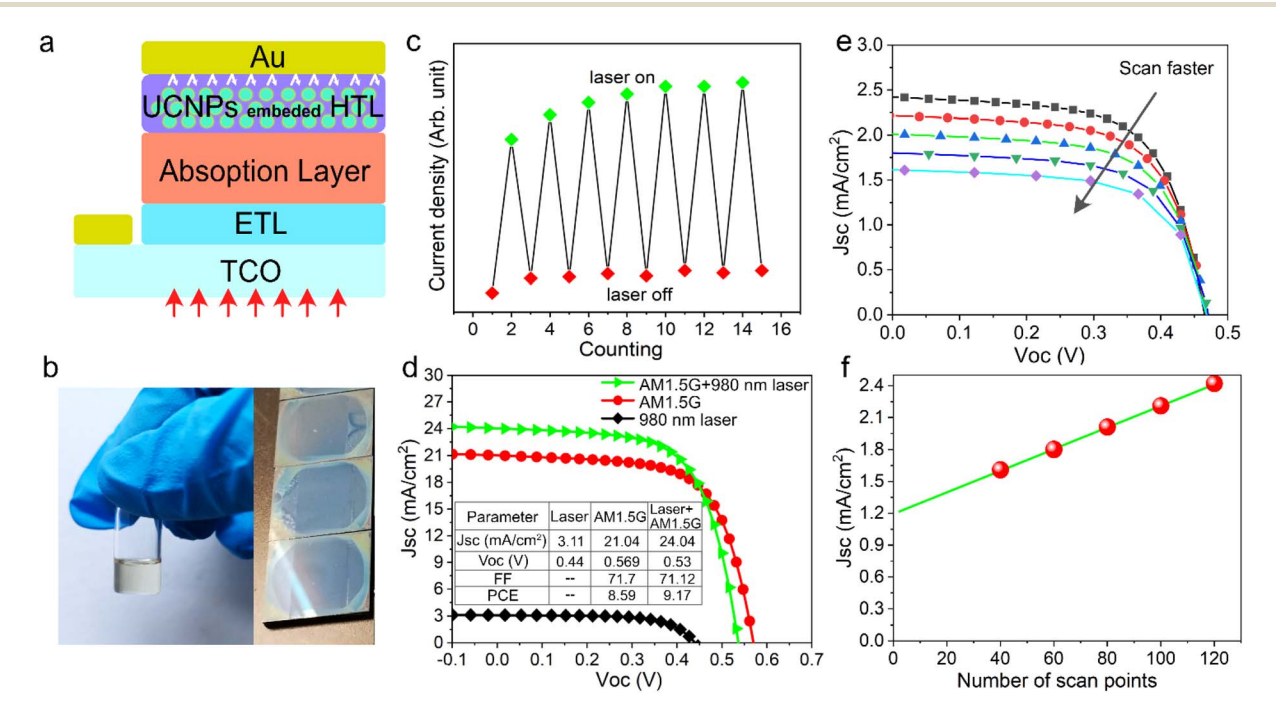


Fig. 4 (a) Schematic illustration of $Sb_2(S,Se)_3$ solar cells using the UCNP-embedded hole transporting layer. (b) Digital photo showing chlorobenzene solution of Spiro-OMeTAD and UCNPs and its coating. (c) Photocurrent of $Sb_2(S,Se)_3$ solar cells tested with continuous sunlight and a 980 nm NIR laser switched on and off. (d) The current density-voltage (J-V) characteristics of $Sb_2(S,Se)_3$ solar cells under AM 1.5G sunlight, a 980 nm laser and their combination. (e) J-V characteristics of solar cells tested under a solo laser with different scan rates (controlled by the number of scan points). (f) Plot of short circuit current density *versus* the number of scan points.

S6a†), Sb₂(S,Se)₃ solar cells with added UCNPs show similar performance under AM 1.5G illumination. We believe that the primary reasons are the limited quantum efficiency and narrow absorption band of Yb3+, which are common problems faced by current rare earth-doped UCNPs. In addition, the infrared photons in sunlight that can be captured by UCNPs carry a limited amount of energy. Therefore, it is necessary to consider the practical operating environment required for such a synergistic energy conversion device combining solar cells and upconversion luminescence in order to obtain appreciable performance gains. It can be seen that the short-circuit current density increases from 21.04 mA cm⁻² to 24.04 mA cm⁻² and the device attained a nominal power conversion efficiency of 9.17% under additional NIR laser irradiation. To make the conclusions more rigorous, we further tested the photocurrent of the solar cell under a 980 nm laser and at different scan rates (Fig. 4e). The short-circuit current density was found to decrease gradually with an increasing scan rate, suggesting the existence of another pathway contributing to photocurrent gain in addition to the UCL process. We speculate that this was due to the non-negligible thermal effect caused by the nonradiative transition of UCNPs when absorbing high-energy lasers. This is indirectly evidenced by the slight drop in the open circuit voltage as shown in Fig. 4d. As shown in Fig. 4f, we can extrapolate the photocurrent gain originating from upconversion luminescence to be about 1.2 mA cm⁻², which indicates that thermal dissipation should be fully considered when introducing UCNPs into solar cell devices operating under concentrated sunlight irradiation.

Conclusions

In summary, we have efficiently synthesized monodisperse hexagonal NaYF4 host crystals based on a customized heating strategy. It is shown that the thermal history and growth temperature jointly determine the final morphology, size and crystal structure of the nanocrystals. Based on the optimal synthesis parameters, we successfully prepared a variety of UCNPs with a core-shell-shell structure doped with different lanthanides, in which the growth and luminescence properties of UCNPs based on an Er3+ activator and a Yb3+ sensitizer were investigated in detail. It was found that the emission can switch between green, yellow and red depending on the excitation power density. The red emission was further shown to be produced from a three-photon process associated with crossrelaxation between neighbouring Er3+ ions due to the highly doped Er³⁺ in the core. Finally, we further introduced the synthesized UCNPs into Sb₂(S,Se)₃ solar cells, and the results confirmed that the photocurrent can be effectively promoted by the UCNPs.

Experimental details

Synthesis of lanthanide-doped UCNPs with a core-shell-shell structure

In this study, UCNPs were prepared by the thermal decomposition method. For a typical synthesis procedure of NaYF4

crystals, 0.1 g of Y₂O₃ was dissolved in 2 ml of deionized water and 4 ml of trifluoroacetic acid (TFA, 87%) in a three-neck flask. The mixture was heated at 90 °C with magnetic stirring to form transparent solution. Then metal-TFA precursor powder was obtained by evaporating the water at 120 °C. Subsequently, 0.34 g of CF₃COONa, 10 ml of oleic acid (OA) and 10 ml of 1octadecene (ODE) were added into a flask which was connected to a Schlenk Line (Fig. S1†). Then the mixture was heated using a heat jacket controlled by a programmable digital controller. The temperature profile for the whole process was pre-settled. After the program was run, Ar purging and vacuum pumping were conducted alternately in the low temperature region (T <130 °C) to remove residual water and oxygen. The growth of UCNPs was carried out under an Ar gas flow and magnetic stirring. After the reaction was completed, the flask was withdrawn from the heating jacket and quickly cooled to room temperature. The yellowish mixture (shown in Fig. S1†) was precipitated by adding 40 ml of ethanol and then centrifuged at 7000 rpm for 10 min and finally redispersed in 5 ml of cyclohexane. The synthesis procedures for the NaYF₄:10%Er core, NaYbF4 inner shell and NaYF4 outer shell were identical to that for pure NaYF4, except that 1.5 ml of as-prepared NaYF4:10%Er solution, 0.197 g of Yb₂O₃ and 0.34 g of CF₃COONa were used for growing the NaYbF4 inner shell and 2 ml of as-prepared NaYF₄:10%Er@NaYbF₄ core-shell solution, 0.113 g of Y₂O₃, and 0.34 g of CF₃COONa were used for growing the NaYF₄ outer shell. In addition, by replacing the activator with Tm³⁺ and Ho³⁺ NaYF4:10%Tm@NaYbF4 and NaYF4:10% Ho@NaYbF4:40%Ce UCNPs can be prepared in a similar way.

Preparation of Sb₂(S,Se)₃ solar cells based on the UCNP embedded HTL

The detailed fabrication procedure of Sb₂(S,Se)₃ solar cells can be found in our previous work.34 Briefly, the SnO2 electron transporting layer was first prepared by the spin-coating method, followed by the deposition of the CdS layer through the chemical bath deposition process. Then the Sb₂(S,Se)₃ lightabsorbing layer was deposited through the hydrothermal method. It should be noted here that the bandgap of the asprepared Sb₂(S,Se)₃ film is around 1.55 eV. After this, the asprepared UCNPs dispersed in cyclohexane were mixed with Spiro-OMeTAD solution in a ratio of 1:4 by volume. Finally, the above-prepared solution was spin coated onto Sb₂(S,Se)₃ to obtain a bifunctional hole transporting layer.

Characterization of UNNPs and solar cell devices

The crystal structure of UCNPs was examined using an X-ray diffractometer (XRD, Bruker D8 Advance) with Cu-Ka radiation (1.5406 Å). The morphology of nanoparticles was collected by field emission SEM (FE-SEM, JOEL JSM-7600F) attached with a transmission electron detector. We would like to emphasize here that the TED mode is able to obtain test results similar to those of scanning transmission electron microscopy, albeit using a lower (30 kV) accelerating voltage. The microstructure information of nanoparticles was acquired by transmission electron microscopy (TEM, JEOL 2100F). The emission

spectrum was collected by placing the sample in an integrating sphere (Labsphere) and exciting it with a 980 nm laser. The output of the integrating sphere is coupled through an optical fiber to a charge-coupled device (Newton 920 CCD, Andor) in which the photon is captured.

The current density-voltage (J-V) curves of solar cells were collected using a Xe-based light source solar simulator (VS-0852 and KEITHLEY 2612A) to provide simulated AM 1.5G illumination which was calibrated using a standard Si reference cell. The active area of solar cells is defined using a shadow mask of 0.09 cm^2 .

Conflicts of interest

There are no conflicts to declare.

Acknowledgements

This research was supported by the National Research Foundation, Prime Minister's Office, Singapore under its Campus of Research Excellence and Technological Enterprise (CREATE) programme and the Singapore Ministry of Education Tier 1 grant (2020-T1-001-147(RG64/20)).

Notes and references

- 1 B.-S. Moon, T. K. Lee, W. C. Jeon, S. K. Kwak, Y.-J. Kim and D.-H. Kim, *Nat. Commun.*, 2021, **12**, 4437.
- 2 S. Ji, S. Liu, X. Lin, Y. Song, B. Xiao, Q. Feng, W. Li, H. Xu and Z. Cai, ACS Photonics, 2021, 8, 2311–2319.
- 3 S. Bi, Z. Deng, J. Huang, X. Wen and S. Zeng, *Adv. Mater.*, 2022, 2207038, DOI: 10.1002/adma.202207038.
- 4 T. Jia, Q. Wang, M. Xu, W. Yuan, W. Feng and F. Li, *Chem. Commun.*, 2021, 57, 1518–1521.
- 5 R. Singh, E. Madirov, D. Busko, I. M. Hossain, V. A. Konyushkin, A. N. Nakladov, S. V. Kuznetsov, A. Farooq, S. Gharibzadeh, U. W. Paetzold, B. S. Richards and A. Turshatov, ACS Appl. Mater. Interfaces, 2021, 13, 54874–54883.
- 6 J. Jin, Q. Cao, L. Zhao, Y. Zhou, Z. Li, L. Gui, Z. Chen, C. Wu, S. Wang and B. Chi, *Mater. Today Commun.*, 2022, 33, 104513.
- 7 F. Xu, Y. Sun, H. Gao, S. Jin, Z. Zhang, H. Zhang, G. Pan, M. Kang, X. Ma and Y. Mao, ACS Appl. Mater. Interfaces, 2021, 13, 2674–2684.
- 8 J. Roh, H. Yu and J. Jang, ACS Appl. Mater. Interfaces, 2016, 8, 19847–19852.
- 9 D. Zhou, D. Liu, J. Jin, X. Chen, W. Xu, Z. Yin, G. Pan, D. Li and H. Song, *J. Mater. Chem. A*, 2017, 5, 16559–16567.
- 10 B. Liu, C. Li, P. Yang, Z. Hou and J. Lin, *Adv. Mater.*, 2017, **29**, 1605434.

- 11 H. Li, X. Liu and X. Li, RSC Adv., 2019, 9, 42163-42171.
- 12 D. Xu, A. Li, L. Yao, H. Lin, S. Yang and Y. Zhang, *Sci. Rep.*, 2017, 7, 43189.
- 13 A. Hlaváček, Z. Farka, M. J. Mickert, U. Kostiv, J. C. Brandmeier, D. Horák, P. Skládal, F. Foret and H. H. Gorris, *Nat. Protoc.*, 2022, 17, 1028–1072.
- 14 C. Cheng, Y. Xu, S. Liu, Y. Liu, X. Wang, J. Wang and G. De, *J. Mater. Chem. C*, 2019, 7, 8898–8904.
- 15 V. Kale, T. Soukka, J. Hölsä and M. Lastusaari, J. Nanopart. Res., 2013, 15, 1850.
- 16 M. Yuan, R. Wang, C. Zhang, Z. Yang, W. Cui, X. Yang, N. Xiao, H. Wang and X. Xu, J. Mater. Chem. C, 2018, 6, 10226–10232.
- 17 J. Zuo, Q. Li, B. Xue, C. Li, Y. Chang, Y. Zhang, X. Liu, L. Tu, H. Zhang and X. Kong, *Nanoscale*, 2017, **9**, 7941–7946.
- 18 F. Wang, J. Wang and X. Liu, Angew. Chem., Int. Ed., 2010, 49, 7456–7460.
- 19 C. Homann, L. Krukewitt, F. Frenzel, B. Grauel, C. Würth, U. Resch-Genger and M. Haase, *Angew. Chem., Int. Ed.*, 2018, 57, 8765–8769.
- 20 X. Liu, X. Kong, Y. Zhang, L. Tu, Y. Wang, Q. Zeng, C. Li, Z. Shi and H. Zhang, *Chem. Commun.*, 2011, 47, 11957.
- 21 B. Zhou, B. Tang, C. Zhang, C. Qin, Z. Gu, Y. Ma, T. Zhai and J. Yao, *Nat. Commun.*, 2020, 11, 1174.
- 22 Y. Zhu, S. Zhao, B. Zhou, H. Zhu and Y. Wang, *J. Phys. Chem. C*, 2017, **121**, 18909–18916.
- 23 Q. Liu, Y. Zhang, C. S. Peng, T. Yang, L.-M. Joubert and S. Chu, *Nat. Photonics*, 2018, 12, 548–553.
- 24 T. Rinkel, J. Nordmann, A. N. Raj and M. Haase, *Nanoscale*, 2014, **6**, 14523–14530.
- 25 S. Dühnen, T. Rinkel and M. Haase, *Chem. Mater.*, 2015, 27, 4033–4039.
- 26 J. Jia, J. Dong, J. Lin, Z. Lan, L. Fan and J. Wu, J. Mater. Chem. C, 2019, 7, 937–942.
- 27 F. L. Meng, J. J. Wu, E. F. Zhao, Y. Z. Zheng, M. L. Huang, L. M. Dai, X. Tao and J. F. Chen, *Nanoscale*, 2017, 9, 18535–18545.
- 28 J. Liang, H. Gao, M. Yi, W. Shi, Y. Liu, Z. Zhang and Y. Mao, *Electrochim. Acta*, 2018, **261**, 14–22.
- 29 H.-X. Mai, Y.-W. Zhang, L.-D. Sun and C.-H. Yan, *J. Phys. Chem. C*, 2007, **111**, 13721–13729.
- 30 H. Li, X. Shi, X. Li and L. Zong, Opt. Mater., 2020, 108, 110144.
- 31 W. Wang, J. Tian, J. Dong, Y. Xue, D. Hu, W. Hou, H. Tang, Q. Wang, X. Xu and J. Xu, *J. Lumin.*, 2021, **233**, 117931.
- 32 D. T. Klier and M. Kumke, RSC Adv., 2015, 5, 67149-67156.
- 33 T. Trupke, M. A. Green and P. Würfel, J. Appl. Phys., 2002, 92, 4117–4122.
- 34 X. Jin, Y. Fang, T. Salim, M. Feng, Z. Yuan, S. Hadke, T. C. Sum and L. H. Wong, *Adv. Mater.*, 2021, 33, e2104346.